

Locally Synchronized Astrocytes

Takuya Sasaki¹, Nahoko Kuga¹, Shigehiro Namiki^{1,2}, Norio Matsuki¹ and Yuji Ikegaya^{1,3}

¹Laboratory of Chemical Pharmacology, Graduate School of Pharmaceutical Sciences, University of Tokyo, Bunkyo-ku, Tokyo 113-0033, Japan, ²Graduate School of Life and Environmental Sciences, University of Tsukuba, Tsukuba, Ibaraki 305-8572, Japan and ³Precursory Research for Embryonic Science and Technology (PRESTO), Japan Science and Technology Agency, Chiyoda-ku, Tokyo 102-00075, Japan

Address correspondence to Yuji Ikegaya. Email: ikegaya@mol.f.u-tokyo.ac.jp.

Astrocytes exhibit spontaneous calcium fluctuations. These activities have not been captured by large-scale recordings, and little is known about their collective dynamics. In situ and in vivo calcium imaging from hundreds (up to 2195) of astrocytes in the mouse hippocampus and neocortex revealed that neighboring astrocytes spontaneously exhibited synchronous calcium elevations and formed locally correlated cell groups (“clusters” of 2 to 5 astrocytes within a diameter of $81 \pm 45 \mu\text{m}$). Cluster activity accounted for approximately 10% of the astrocytic calcium events, and 44% of the clusters appeared repetitively during our observation period of 60 min. Astrocytic clusters emerged through metabotropic glutamate receptor activation, independently of neuronal activity. Neurons were depolarized by 1.5 mV when clusters appeared near their dendrites. This depolarization was mediated by non-*N*-methyl-D-aspartate (NMDA) glutamate receptor channels and was replicated by calcium uncaging activation of multiple astrocytes. Importantly, the activation of single astrocytes alone could not depolarize neurons but readily elicited NMDA-dependent slow inward currents in depolarized neurons. Thus, these novel ensemble dynamics of astrocytes, which cannot be captured by conventional small-scale imaging techniques, play a different role in neuronal modulation than does the sporadic activity of single astrocytes.

Keywords: astrocyte, calcium, glutamate, network, synchronization

Introduction

The brain functions through coordinated neuron–glial interactions. One form of excitability displayed by astrocytes is a change in the intracellular calcium concentration. In the hippocampus, the astrocytic calcium activity triggers the extracellular release of various “gliotransmitters,” although these observations remain controversial (Fiacco et al. 2007; Agulhon et al. 2010; Hamilton and Attwell 2010). Among the gliotransmitters, for example, glutamate is well known to evoke postsynaptic slow inward currents (SICs) in nearby neurons by activating *N*-methyl-D-aspartate (NMDA) receptors (Araque et al. 1998a; Kang et al. 1998; Angulo et al. 2004; Fellin et al. 2004; Fiacco and McCarthy 2004; Tian et al. 2005; Jourdain et al. 2007; Perea and Araque 2007). Glutamate released from astrocytes also facilitates the neurotransmitter release from presynaptic terminals at excitatory (Fiacco and McCarthy 2004; Jourdain et al. 2007; Perea and Araque 2007) and inhibitory synapses (Araque et al. 1998b; Kang et al. 1998). Studies using acute hippocampal slices reveal that astrocytes respond with calcium elevation to neuronal stimulation and that this activation is mediated by G protein–coupled metabotropic receptors (Dani et al. 1992; Porter and McCarthy 1996; Perea and Araque 2005). Wang et al. (2006) reported that

whisker stimulation in vivo evokes the calcium activity of astrocytes in the barrel cortex in a stimulation frequency-dependent manner. These findings indicate that neurons and astrocytes are mutually responsive to each other.

Interestingly, astrocytes are capable of displaying spontaneous calcium fluctuations, even independent of neuronal activity. A typical form of the calcium activity observed in cell culture preparations is intercellularly traveling waves that propagate over astrocytic networks with a cell-to-cell delay of tens of seconds (Cornell-Bell et al. 1990; Charles et al. 1991; Araque et al. 1998b), whereas little evidence shows those propagating waves in intact cortical brain tissues (Fiacco et al. 2009), except for Bergmann glia in the cerebellum (Hoogland et al. 2009; Nimmerjahn et al. 2009). A more predominant feature of ongoing astrocytic activity seems to be “pairwise synchronization”; the onset timings of the activities of 2 neighboring astrocytes are correlated at a nearly zero time lag. The synchronized activity has been described in acute hippocampal slices (Aguado et al. 2002; Nett et al. 2002) and the in vivo neocortex (Hirase et al. 2004; Takata and Hirase 2008; Kuchibhotla et al. 2009).

In all these previous studies, however, calcium activity has been recorded from only a small number of astrocytes (up to 40 cells) and for short periods of time such as 10 min. Therefore, the large-scale spatiotemporal structures of astrocytic activity are poorly defined. In this study, we monitored hundreds of astrocytes in situ and in vivo for 60 min and found a novel ensemble behavior in which a few adjacent astrocytes exhibited synchronous calcium activities that yielded active multicellular domains of astrocytes. In a few cases, we observed globally synchronized wave-like activity in vivo. Data including the global activity were excluded from the analyses in the present study and reported in another paper (Kuga et al. 2011).

Materials and Methods

All experiments were carried out in accordance with the Japanese Pharmacological Society guide for the care and use of laboratory animals. Data are reported as the means \pm standard deviations (SD), unless otherwise specified. Tetrodotoxin, picrotoxin, L,D-2-amino-5-phosphonopentanoic acid (AP5), 6-cyano-7-nitroquinoxaline-2,3-dione (CNQX), (*S*)- α -methyl-4-carboxyphenylglycine (MCPG), 18- β -glycyrrhetic acid (18 β -GA), suramin, and adenosine 3'-phosphate 5'-phosphosulfate (PAPS) were bath applied. These reagents were all purchased from Sigma-Aldrich.

Hippocampal Slice Preparation

Postnatal 9- to 12-days-old ICR mice (SLC) were anesthetized with ether and decapitated. The brain was immersed in ice-cold modified artificial cerebrospinal fluid (aCSF) consisting of (in millimolar) 27 NaHCO₃, 1.4 NaH₂PO₄, 2.5 KCl, 0.5 ascorbic acid, 7.0 MgSO₄, 1.0 CaCl₂, and 222 sucrose, bubbled with 95% O₂ and 5% CO₂. Horizontal entorhinal-hippocampal slices of 400 μm thickness were cut using

a vibratome (Vibratome 3000; Vibratome) and maintained for >60 min at room temperature in normal aCSF consisting of (in millimolar): 127 NaCl, 26 NaHCO₃, 1.6 KCl, 1.24 KH₂PO₄, 1.3 MgSO₄, 2.4 CaCl₂, and 10 glucose. For calcium uncaging experiments, postnatal day 7 Wistar/ST rats were chilled with ice and decapitated. The brains were removed and horizontally cut into 300- μ m-thick slices using a DTK-1500 vibratome (Dosaka) in aerated, ice-cold Gey's balanced salt solution supplemented with 25 mM glucose. Entorhino-hippocampal stumps were excised and cultivated on Omnipore membrane filters (JHWP02500; Millipore) that were laid on plastic O-ring disks (Koyama et al. 2007). The cultures were fed with 1 ml of 50% minimal essential medium, 25% Hanks' balanced salt solution, 25% horse serum (Cell Culture Laboratory), and antibiotics in a humidified incubator at 37 °C in 5% CO₂. The medium was changed every 3.5 days.

In Situ Calcium Imaging from Hippocampal Slices

Slices were incubated for 40 min at 37 °C with 0.0005% Oregon Green 488 BAPTA-1 (OGB-1) AM (Invitrogen), 0.01% Pluronic F-127 (Invitrogen), 0.005% Cremophor EL (Sigma-Aldrich), and 100 μ M sulforhodamine 101 (SR101; Invitrogen) and then recovered in aCSF for >30 min. After being perfused in a recording chamber with aCSF for >15 min, we initiated the imaging of spontaneous calcium signals from astrocytes in CA1 stratum radiatum and stratum lacunosum-moleculare. Images were captured at 1 Hz with Nipkow-disk confocal microscopy (CSU-X1; Yokogawa Electric), a cooled CCD camera (iXonEM⁺ DV897; Andor Technology), an upright microscope with a \times 0.63 intermediate magnification lens (AxioSkop2; Zeiss and ECLIPSE FN1; Nikon), and a water-immersion objective lens (\times 20, 1.0 numerical aperture, Zeiss; \times 16, 0.8 numerical aperture, Nikon; \times 10, 0.5 numerical aperture, Nikon). For imaging from neocortical slices, an objective (\times 4, 0.2 numerical aperture; Nikon) and a cooled CCD camera (iXonEM⁺ DV888DCS-BV; Andor Technology) were used (Namiki et al. 2009). Fluorophores were excited with an argon laser (wavelength, 488 nm). No grid sinker was used to reduce the slice movement because it bent the surface of the preparation and made it difficult to attain wide microscopic field observations. No off-line compensation was made to adjust the movement of slice preparations. Instead, data were discarded when the imaged region drifted >5 μ m during 60 min of our imaging period. As a result, we used only ~20% of the tested slices in the following analyses. To apply electric stimulation, glass pipettes were filled with aCSF and placed in CA1 stratum radiatum, and single-pulse or burst-train stimuli at 100 Hz (each 80 μ s at 100–200 μ A) were applied at intervals of >30 s.

In Vivo Calcium Imaging of Hippocampal Astrocytes

Male ICR mice (postnatal 12–22 days old) were anesthetized with urethane (1.5 g kg⁻¹, i.p.), and the exposed skull was glued to a metal plate, which was fixed to a stereotaxic frame (Fig. 5A). A craniotomy (2.5–3 mm diameter), centered at 2.5 mm posterior and 2.2 mm lateral to the bregma, was performed, and the dura was surgically removed. According to Mizrahi et al. (2004), the cortical tissue above the hippocampus was removed by aspiration (Fig. 5B). Then, the exposed dorsal surface of the hippocampus was loaded with a small volume (about 2 μ l) of dye solution that consists of 0.125% fluo-4AM (Invitrogen), 100 μ M SR101, 20% DMSO, and 8% Pluronic F-127. During an incubation period of 45–60 min, the hippocampal surface was covered with a small piece of Gel Form (Pfizer Inc.), so that the dye solution was retained in place. With this method, fluo-4-loaded cells were almost exclusively SR101-positive astrocytes (Fig. 5C). After the unloaded dye was washed with aCSF, the aspirated area was mounted with 2% agar dissolved in aCSF. Astrocytic calcium activity was imaged with a 2-photon laser-scanning microscope based on a mode-locked Ti:sapphire laser with a 100 fs pulse width, 80 MHz pulse frequency, and 840 nm wavelength (Maitai; Spectra Physics), an upright microscope (BX61WI; Olympus), and a water-immersion objective lens (\times 20, 0.95 numerical aperture; Olympus). After each experiment, the brain was removed and immediately frozen. Coronally sectioned preparations (30 μ m thickness) were stained with 0.1% Cresyl Fast Violet (Wako Pure Chemical Industries) to confirm the imaged area. For drug application, calcium activities were monitored during a control period, and the agar that covered the

hippocampus was carefully torn away. The hippocampal surface was perfused with drugs for 10 min and covered again with 2% agar containing the drugs at the same concentration used for perfusion. The drugs were dissolved in the agar solution immediately before covering.

Analysis of Calcium Dynamics

The cell bodies of astrocytes were carefully identified by eye to put the regions of interest (ROIs). Astrocytic endfeet were also labeled with calcium dyes, and thus, we carefully avoided placing ROIs on the labeled endfeet, based on 2 following features. First, the somata of astrocytes are almost uniformly separated at a cell-to-cell distance of 40–50 μ m (Supplementary Fig. S1), and the ROIs were not placed within 30 μ m from the nearest ROIs. Second, some types of astrocytes contact vessels through their endfeet, and these endfeet are easily identified by eye (see the lower part of Supplementary Movie 1). Moreover, to minimize signal contaminations from astrocytic processes, the ROI size was set to 10 μ m in diameter, which corresponds to the size of the astrocytic soma. In each ROI, the fluorescence intensity was spatially averaged. The fluorescence change was defined as $\Delta F/F = (F_t - F_0)/F_0$, where F_t is the fluorescence intensity at time t , and F_0 is the baseline averaged for 50 s before and after time t . Calcium rises were extracted with the thresholds of 4 SD of baseline noise and a 5-s duration.

Cross-correlations were calculated as $R_{i,j}(\tau) = \int f_i(t)f_j(t+\tau)dt$, where $f_i(t)$ represents the normalized fluorescence signal of cell_{*i*}. The time lag τ ranged from -10 to 10 s, during which period the maximal $R_{i,j}(\tau)$, termed the maximal cross-correlation (MCC) value, was used as an index of similarity in calcium dynamics between cell_{*i*} and cell_{*j*}. By calculating MCCs for all possible pairs, we obtained the MCC matrix. For each matrix, a graph that represents the functional connectivity was drawn by extracting strongly correlated pairs that had MCCs greater than a specific threshold (see below) and by connecting them with arrows (directed edges). The arrow directions were determined based on the signs of the time lags that gave the MCCs. If the time lags were zero, the pairs were bidirectionally connected. For the total number of extracted cells (N) and the number of extracted connections (K), the edge density was defined as the ratio of K to the maximal possible number, that is, $K/\{N \times (N-1)\}$. The threshold to extract a graph was determined to minimize the edge density (Fig. 2F) because at this point the graph conveys the maximal information about its complex topology (Royer et al. 2008). In our study, the MCC threshold was 0.62 ± 0.16 , and the edge density at the threshold was 0.17 ± 0.16 ($n = 9$ slices from 7 animals).

To evaluate the “small-worldness” of a graph, the global efficiency E (Latora and Marchiori 2001) and the clustering coefficient C (Watts and Strogatz 1998) were compared to those of 100 equivalent random graphs in which edges are randomly rewired while maintaining N and the total numbers of each bidirectional and unidirectional connections. For a small-world graph, we expect the ratio $\lambda = E/E_{\text{random}}$ to be approximately 1 and the ratio $\gamma = C/C_{\text{random}}$ to be >1. Therefore, a scalar measure of small-worldness is defined as $\sigma = \gamma \times \lambda$, which is >1 if the network exhibits small-world attributes (Humphries et al. 2006). The MCC matrix was also analyzed with the affinity propagation algorithm (Frey and Dueck 2007) to identify astrocytic cliques based on their correlations. The spatial dispersion of the positions x_i ($i = 1, 2, \dots, N$) of the cells that belonged to the same subgroup was evaluated with their mean Euclidean distance to the center of gravity $\bar{x} = \sum x_i/N$, that is, $\sum \sqrt{(x_i - \bar{x})^2}/N$. The dispersion was compared to that of 1000 random cell maps in which the group identity of individual cells was randomly shuffled across groups.

Three-Dimensional Simulation of Astrocyte Activity

To estimate the true size and density of astrocytic clusters, the stereoscopic activity patterns of astrocytes were reconstructed through computer simulation with a random percolation procedure. In a 450 \times 450 \times 450- μ m cubic space, 1416 astrocytes were uniformly placed at the apexes of the hexagonal close-packed lattice. Based on our observation of Supplementary Figure S1, the cell-to-cell interval was set to be 50 μ m. Then, MCC values were randomly assigned for all cell pairs to meet both the MCC distribution and its cell-to-cell

distance relationship in Figure 2*B–D*. In each trial of simulation, 1 cell is randomly selected, and the rest of the cells are stochastically activated along the MCC-weighted edges from the selected cell (percolation). A cell is considered to be active if the MCC exceeds a randomly generated value that ranged from 0 to 1. The simulation was iterated 100 times for each MCC matrix. In the simulation, a threshold was put on the MCC matrix, above which edges are used in the percolation process. This threshold was determined in a range from 0.15 to 0.25 for each MCC matrix, so that the distribution of the number of cells involved in single clusters and the percentage of cluster-participating calcium activity were closest to those of the real confocal data when the simulation data were “pseudoconfocally” sectioned into a randomly selected 25- μm -thick plane across the 3D lattice. In other words, we intended to estimate the 3D dynamics of astrocytic clusters by adjusting the threshold parameter so as to fit them to our confocal 2D movies. The simulation was performed with custom software written in Matlab (Mathworks).

Immunohistochemistry

Slices were fixed in 4% paraformaldehyde in 0.1 M phosphate buffer solution for 2 h and permeabilized with 0.3% Triton X-100 for 60 min. After being blocked by a 60-min incubation with 2% goat serum at 4 °C, they were incubated with primary mouse monoclonal anti-NeuN antibody (1:1000; Chemicon International), rabbit monoclonal anti-S100 β antibody (1:1000; Swant Swiss Antibodies), and mouse monoclonal anti-CD31 antibody (1:100; BD Pharmingen) overnight at 4 °C and labeled with the secondary anti-rabbit IgG Alexa-488 (1:400; Invitrogen) and anti-mouse IgG Alexa-594 (1:1000; Invitrogen) for 6 h at room temperature. Images were acquired at a Z-depth interval of 5 μm with a 2-photon laser scanning system.

Electrophysiological Recording and Calcium Uncaging

Patch-clamp recordings from hippocampal slice cultures were carried out with a MultiClamp 700B amplifier and a Digidata 1440A digitizer controlled by pCLAMP 10 software (Molecular Devices). Borosilicate glass pipettes (7–9 M Ω) were filled with internal solution consisting of (in millimolar): 135 K-gluconate, 4 KCl, 10 4-(2-hydroxyethyl)-1-piperazineethanesulfonic acid, 10 phosphocreatine- Na_2 , 0.3 Na_2 -GTP, and 4 Mg-ATP (pH 7.2). To patch-clamp astrocytes, 100 μM OGB-1 potassium salt (Invitrogen), 200 μM *o*-nitrophenyl-ethyleneglycol-bis(2-aminoethylether)-*N,N,N',N'*-tetra acetic acid (NP-EGTA; Invitrogen), and 10 mM glucose are added to the pipette solution. For neuron recording, 200 μM Alexa Fluor 488 hydrazide (Invitrogen) was added to the pipette solution. Cell types were identified by checking the electrophysiological and morphological properties typical of neurons and astrocytes. Astrocytes had more negative resting membrane potentials (-82 ± 4.2 mV, $n = 10$ cells) than neurons (-65 ± 4.9 mV, $n = 10$ cells), received no spontaneous fast synaptic inputs, and did not fire action potentials even when strong depolarizing currents (500 pA for 500 ms) were injected. Moreover, the diameter of astrocytic somata was <10 μm , bearing no long processes. Signals were low-pass filtered at 1–2 kHz, digitized at 10 kHz, and were analyzed with pCLAMP 10 software. NP-EGTA was uncaged by 30–120 s exposures of ultraviolet (UV) light, which was emitted from a 100-mW high-pressure mercury lamp (C-SHG1; Nikon) and short-passed at 330 nm (XF1001; Omega Optical). For uncaging experiments, we utilized organotypic slice preparations because they were more suitable to photostimulation of the selected cells, compared with acute slices, due to higher transparency of brain parenchyma and less cellular debris on the preparation surface, which both reduce the scattering of short-wavelength light, such as UV.

Results

Uniform Alignment of Hippocampal Astrocytes

As an initial step in investigating the dynamics of multiple astrocytes, we examined the spatial alignment of astrocytes in brain tissues. Acute hippocampal slices were immunolabeled with S100 β , an astrocyte marker, and the spatial distribution

of individual astrocytes was observed using 2-photon microscopy. The mean cell-to-cell distance ranged from 40 to 50 μm , and the cell density was $17.0 \times 10^3 \pm 2.5 \times 10^3 \text{ mm}^{-3}$, consistent with another quantitative analysis (Ogata and Kosaka 2002). Astrocytes were positioned evenly, rather than randomly, in the hippocampus (Supplementary Fig. S1). This finding corresponds with a report showing that the processes of astrocytes do not overlap one another but establish exclusive territories (Bushong et al. 2002).

Spontaneous Calcium Dynamics in Astrocytes

Hippocampal slices were incubated with OGB-1AM and SR101. SR101-positive cells in the CA1 stratum radiatum and lacunosum-moleculare were S100 β immunopositive (Fig. 1*A*) (Nimmerjahn et al. 2004). Calcium events were time-lapse imaged using a Nipkow-disk confocal system. On average, single movies included 156 ± 69 astrocytes. An example movie is presented in Figure 1*B*. In control slices, astrocytes exhibited spontaneous calcium activity. During a given 10 s, $4.4 \pm 2.3\%$ astrocytes were active (mean \pm SD of 10 slices from 8 animals). This ratio increased to $85 \pm 19\%$ astrocytes for a period of 60 min (Fig. 1*C*), indicating that most of the astrocytes in our preparations were alive. The overall frequency of astrocytic calcium events did not change over 60 min (Fig. 1*D*), which suggested that no apparent photoexcitation or phototoxicity had occurred.

The mean percentage of astrocytes demonstrating calcium activity during a given minute and the mean frequency, duration, and amplitude of the calcium events are summarized in Figure 1*E–H*. In this work, we pooled all the data obtained from different postnatal ages because we did not find significant age-dependent differences in these parameters at least in the range of animals' ages used here; for example, the percentage of active cells and the frequency of calcium signals were, respectively, $9.3 \pm 3.8\%$ and $0.17 \pm 0.03 \text{ min}^{-1}$ on postnatal day 9 ($n = 12$ slices from 8 animals) and $9.4 \pm 2.6\%$ and $0.18 \pm 0.05 \text{ min}^{-1}$ on postnatal day 12 ($n = 12$ slices from 8 animals). Consistent with previous reports (Aguado et al. 2002; Nett et al. 2002; Takata and Hirase 2008; Kuchibhotla et al. 2009), none of these parameters was affected by 1 μM tetrodotoxin, a voltage-sensitive sodium channel blocker (Fig. 1*E–H*).

Local Correlations of Astrocytic Calcium Activities

Observation of the time-lapse movie revealed that some of the astrocytic activities were locally correlated (Movie 1). This motivated us to quantify the functional interaction among astrocytes. We computed the cross-correlation function between the calcium traces of 2 astrocytes and adopted the MCC value within a time lag of ± 10 s as a measure of similarity between the waveforms (Fig. 2*A*). A representative MCC matrix is illustrated in Figure 2*B*. The rank-order distribution of the top 10% MCCs, separated along the cell-to-cell distance, demonstrated that the more closely located cells showed a stronger correlated activity (Fig. 2*C*). This trend held true for tetrodotoxin-treated slices (Fig. 2*C*). The distribution of the time lags at which the MCCs were given indicated that astrocytic activity was mostly synchronized with a 0-s delay time (Fig. 2*D*). The same results were obtained using tetrodotoxin-treated slices (Fig. 2*D*).

To avoid human bias, we further employed 2 different mathematical approaches. First, we applied the affinity

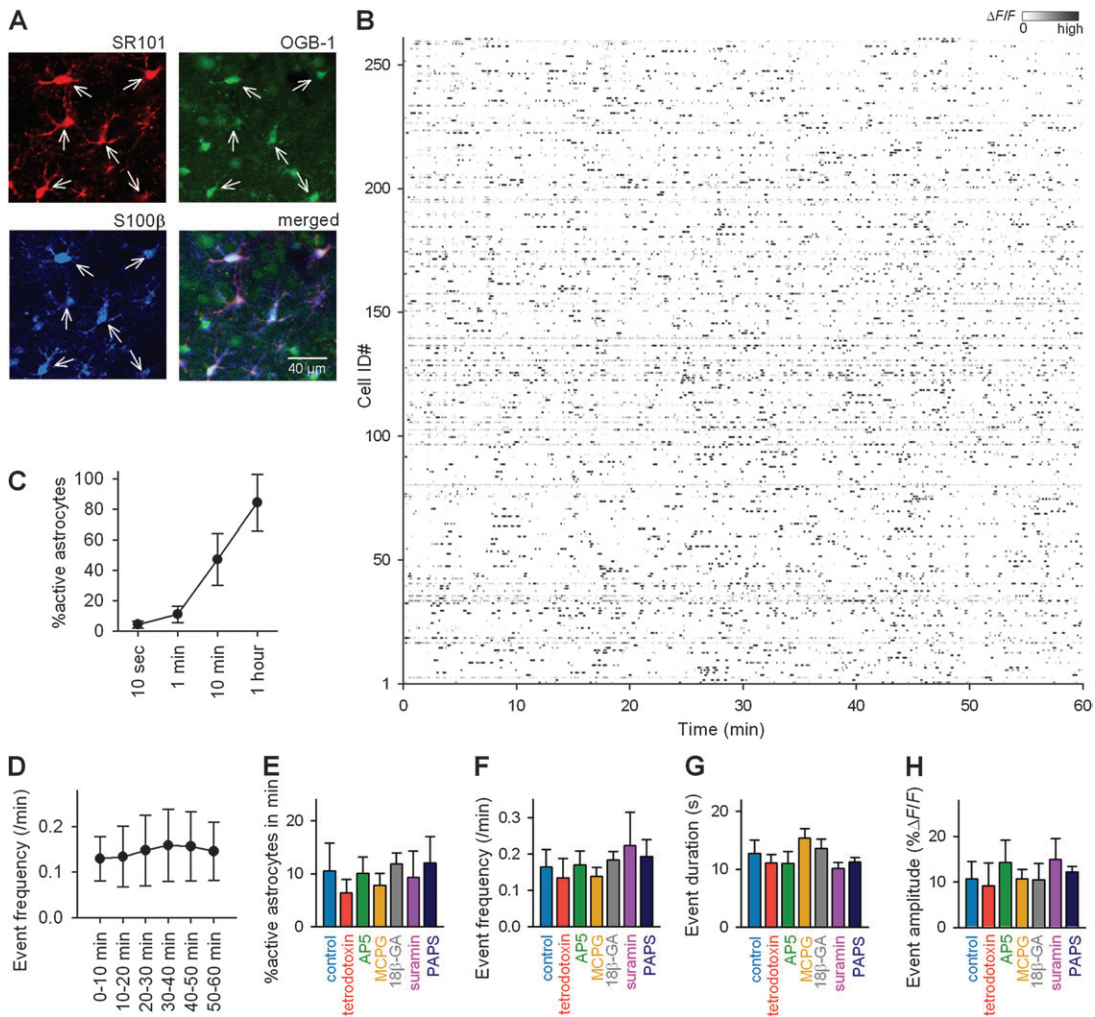


Figure 1. Spontaneous calcium dynamics of large astrocyte populations in situ. (A) Confocal images of astrocytes loaded with SR101 and OGB-1 and postimmunolabeled post hoc with S100 β . Arrows indicate triple-positive cells. (B) Spontaneous calcium fluctuations of 261 astrocytes for 60 min. The fluorescence intensity was normalized to the maximum amplitude in each cell (gray scaled). (C) The mean percentage of active astrocytes in 10-s, 1-min, 10-min, and 60-min time windows ($n = 6-10$ slices from 6 to 8 animals). (D) Time changes in the frequency of astrocytic calcium events in each 10 min during 60 min of our observation period. (E-H) The percentage of active astrocytes in a given minute (E) and the frequency (F), duration (G), and amplitude (H) of calcium transients in control ($n = 1592$ cells from 10 slices from 8 animals), 1 μ M tetrodotoxin-treated ($n = 1136$ cells from 6 slices from 5 animals), 50 μ M AP5-treated ($n = 586$ cells from 5 slices from 3 animals), 500 μ M MCPG-treated ($n = 615$ cells from 5 slices from 3 animals), 100 μ M 18 β -GA-treated ($n = 709$ cells from 5 slices from 4 animals), 100 μ M suramin-treated ($n = 728$ cells from 5 slices from 3 animals), and 100 μ M PAPS-treated ($n = 798$ cells from 5 slices from 3 animals) preparations.

propagation algorithm (Frey and Dueck 2007) to the MCC matrices and subdivided the astrocyte population. Representative subgroups are shown in Figure 2E, left. The spatial dispersion of within-subgroup cells, the mean distance from the cells to the subgroup center of gravity, was significantly smaller than chance (Fig. 2E, right, $P < 0.05$, Kolmogorov-Smirnov test), indicating that synchronized astrocytes were spatially clustered.

Next, the network topology underlying the MCC matrix was examined using the graph theory. We selected strongly correlated cell pairs by thresholding the MCC values (Fig. 2F) and depicted a directed graph (Fig. 2G). We analyzed the statistics of 3-cell connection patterns called “motifs” (Song et al. 2005). For each motif, the observed counts were compared with the expected counts in the randomly rewired graph (Fig. 2H). Several patterns (motifs #7-13) were overrepresented, suggesting a topologically clustered pattern in the connectivity. Similar results were obtained from tetrodotoxin-treated slices (Fig. 2H).

Consistent with these results, the small-worldness of the MCC graph was significantly higher than chance in both control and tetrodotoxin-treated slices (Fig. 2J).

All these analyses disclosed, without any prior assumption about graph patterns, that the correlated activities of astrocytes were topologically clustered.

Statistical Significance of Astrocytic Clusters

After obtaining the strong mathematical support for the local correlation of astrocytes, we now defined a set of locally synchronous astrocytes, termed “clusters,” as a group of cells that were coactivated within 2 s and within a cell-to-cell distance of 50 μ m, unless otherwise specified (Fig. 3A,B). This “fixed” threshold of the spatial interval for cluster detection is valid because 1) the spacing of astrocytes is uniform (Supplementary Fig. S1) and 2) the statistical difference between real and shuffled datasets was maximized at the detection thresholds of 50 μ m (Fig. 3E). However, it should be noted that the

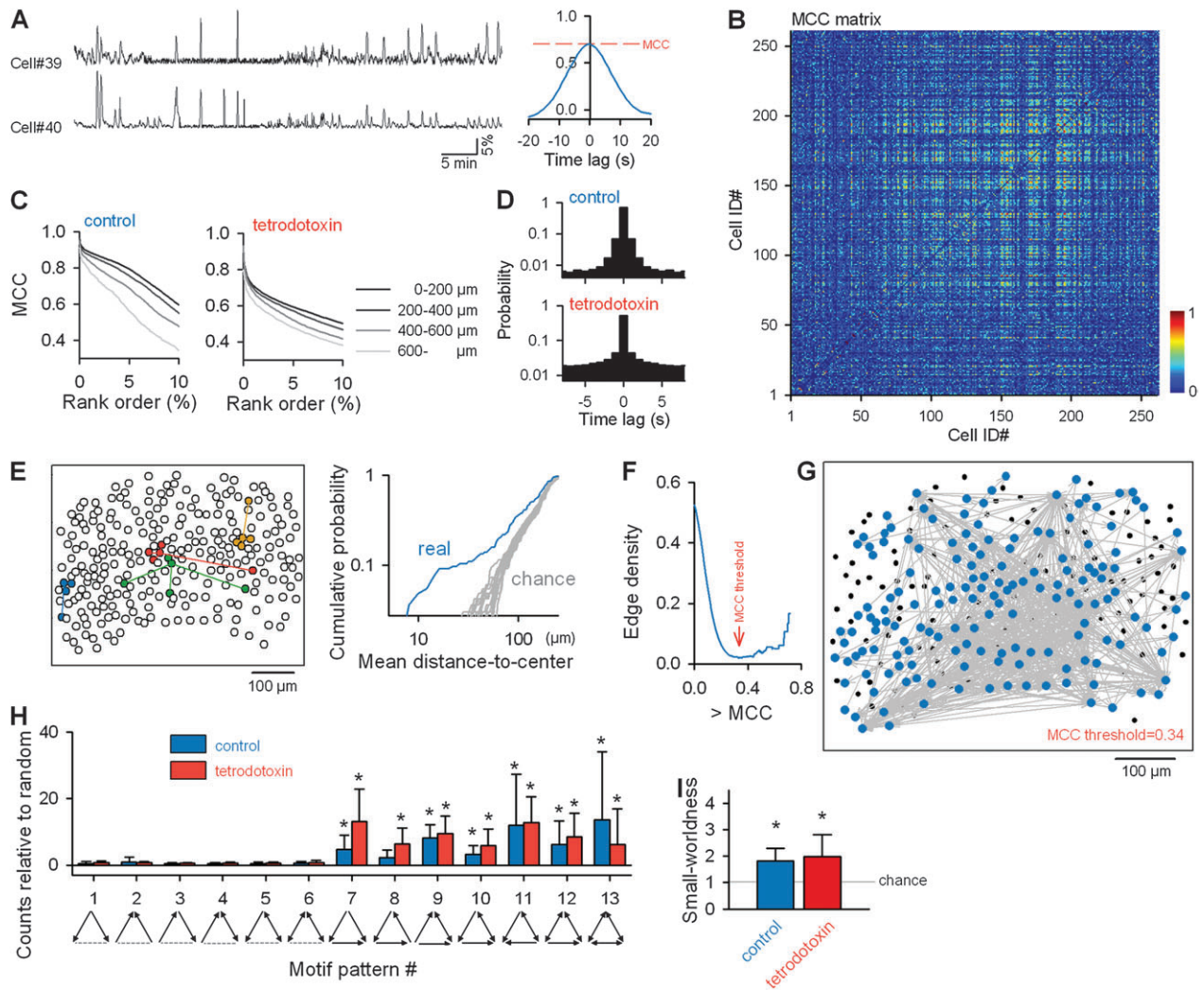


Figure 2. Locally synchronized activity of astrocytes. (A) Representative calcium traces of 2 neighboring astrocytes (left) and their cross-correlogram (right), in which the maximal value was defined as MCC. (B) Pseudocolored MCC matrix of the Figure 1B movie. (C) Rank-order MCC distributions in control and tetrodotoxin-treated slices. The top 10% pairs are plotted separately along the cell-to-cell distance. (D) Distribution of the time lags that gave MCCs in control and tetrodotoxin-treated slices. (E) Cell maps of the astrocyte subgroups identified with affinity propagation (left). Four subgroups are randomly selected for illustration purposes. Each color represents a single subgroup. Cumulative distribution of the mean distance from within-subgroup cells to the subgroup center was compared with that of the random surrogates (right). (F) Effect of graph-extraction thresholds on the edge density of the graphs extracted from a MCC matrix. (G) A graph was extracted at the threshold that gave the lowest edge density (arrow in (F)). In this case, the threshold was 0.34. Data of (F) and (G) were obtained from (B). (H) Ratio of the actual count to the count expected by chance for each 3-cell motif pattern. (I) Small-worldness of MCC matrix. Control ($n = 10$ slices from 8 animals) and $1 \mu\text{M}$ tetrodotoxin-treated slices ($n = 6$ slices from 5 animals). $*P < 0.05$ versus chance, Welch test.

significant overrepresentation was kept significant at thresholds of up to $200 \mu\text{m}$ ($P < 0.01$), suggesting that a few larger islands also existed in astrocytic networks.

During the 60-min observation period, 33 ± 21 clusters emerged per 100 cells (Fig. 3F). Each cluster consisted of 2 to 5 astrocytes within a diameter of $81 \pm 45 \mu\text{m}$. Clusters occupied $9.6 \pm 5.8\%$ of all calcium transients observed (Fig. 3G). Because this ratio of cluster participants appeared to be low (i.e., only about 10%), we suspected that the clusters merely reflected a random coincidence of independent calcium activities. To verify this possibility, we randomized the raster plots of astrocytic calcium events (Ikegaya et al. 2004; Sasaki et al. 2007). A calcium event in a given cell was exchanged with a randomly selected event in another randomly selected cell, and this event swapping was repeated for all events (Fig. 3C, inset). This procedure preserved both the event frequencies of individual cells and the population modulation of event timings.

Twenty surrogates were created for each original dataset. There were significantly fewer clusters in the shuffled datasets than in the real datasets (Fig. 3C). The data are summarized in Fig. 3D ($P = 0.0008$, paired t -test, $n = 9$ slices from 7 animals). The same analysis was repeated with different thresholds of the cell-to-cell distance for cluster detection (Fig. 3E). As mentioned above, a statistically significant difference ($P < 0.01$) was consistently found for the thresholds in the range from 25 to $200 \mu\text{m}$, with the greatest difference observed at $50 \mu\text{m}$. Thus, the existence of clusters cannot be explained by chance, although clusters accounted for only 10% of the astrocytic calcium events.

Astrocytic Clusters as a Nonartificial Phenomenon

It is unlikely that the clusters reflected a gap junction-mediated escape of calcium fluorescence between neighboring cells because OGB-1 is a large molecule of $>1.1 \text{ kDa}$ so that it

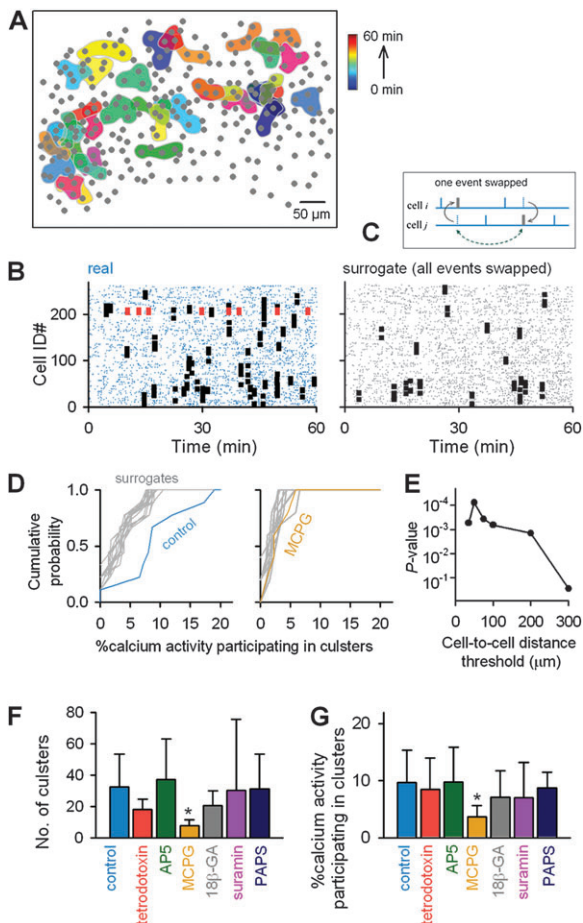


Figure 3. Astrocytic clusters. (A,B) Clusters, shown in the movie in Figure 1B, are shown in a time-changing pseudocolor scale (A) and superimposed on a raster plot of astrocytic activity (B). Only clusters containing more than 2 cells are shown. Red-colored activities represent a repetitively activated cluster. (C) Fewer clusters were found in event-shuffled surrogates than in the real raster plot. (D) Cumulative distributions of the percentage of calcium events participating in clusters were compared with those in the surrogates (gray lines). Left, control ($n = 9$ slices from 7 animals); right, 500 μM MCPG-treated slices ($n = 5$ slices from 3 animals). (E) P value obtained for the percentage of calcium activities involved in clusters relative to that in the surrogates. The P values were determined using the paired t -test by comparing the original data obtained for control slices and their shuffled surrogates ($n = 9$ slices), which were plotted versus the cell-to-cell distance threshold used for cluster detection. (F,G) The number of clusters observed per 100 cells in 60 min (F) and the ratio of the calcium transients participating in clusters to the total transients (G) in the control ($n = 9$ slices from 7 animals), 1 μM tetrodotoxin-treated ($n = 6$ slices from 5 animals), 50 μM AP5-treated ($n = 5$ slices from 3 animals), 500 μM MCPG-treated ($n = 5$ slices from 3 animals), 100 μM 18 β -GA-treated ($n = 5$ slices from 4 animals), 100 μM suramin-treated ($n = 5$ slices from 3 animals), and 100 μM PAPS-treated slices ($n = 5$ slices from 3 animals). * $P < 0.05$ versus control, analysis of variance followed by Tukey's test.

cannot diffuse through a gap junction; note that gap junctions usually allow the exchange of molecules with a molecular mass of <1 kDa (Weber et al. 2004). For confirmation, however, we examined this possibility under our experimental conditions. We microinjected a mixture of OGB-1 and NP-EGTA, a UV-sensitive caged-calcium compound, into single astrocytes through whole-cell patch-clamp pipettes (Supplementary Fig. S2). No leak or spreading of the OGB-1 fluorescence from the patch-clamped cell was detected 15 min after whole-cell break-in. The UV photolysis of NP-EGTA induced an increase in calcium fluorescence, but the increased fluorescence remained

inside the cell (Supplementary Fig. S2). We repeated this experiment in 5 other slices and obtained similar results.

It is possible that an astrocyte that contacted nearby vessels appeared as if it had multiple somata, depending on the angle of view. To examine how astrocytic clusters are geometrically related to the vessel vasculature, 3 slices used in time-lapse calcium imaging were double immunolabeled with S100 β and CD31, a marker of vascular endothelial cells, and compared the vessel alignment to the locations of cells that participated in clusters (Supplementary Fig. S3). We found no specific spatial relationship between the cluster participants and the vessel architectures. Moreover, $97.6 \pm 1.6\%$ of the somata of astrocytes selected for ROIs did not contact vessels. Thus, the “multiple-somata” artifact, if any, did not significantly affect our quantitative data.

Taken together, we concluded that astrocytic clusters are a biologically active phenomenon rather than an artifact of imaging experiments.

Astrocytic Clusters in Neocortex

The present work focused on the hippocampus, but we also discovered similar cluster activity in the neocortex ($n = 4$ slices from 2 animals). A representative movie of a neocortical slice, in which 2195 astrocytes were simultaneously monitored, is presented in Supplementary Fig. S4 and Movie 2.

On the Mechanism Underlying Astrocytic Clusters

We applied pharmacological inhibitors of extracellular signals known to mediate glia-to-glia communication (Agulhon et al. 2008): 50 μM AP5, an NMDA receptor antagonist; 500 μM MCPG, a group I and II metabotropic glutamate receptor antagonist; 100 μM 18 β -GA, a gap junction inhibitor; 100 μM suramin, a broad purinergic receptor antagonist; and 100 μM PAPS, a purinergic P2Y $_1$ receptor antagonist. Although none of these inhibitors altered the properties of spontaneous calcium activity per se (Fig. 1E–H), MCPG attenuated cluster activity to the chance level (Fig. 3D, right, F,G).

Temporal Dynamics of Astrocyte Connectivity

The MCC and its time lag between astrocytes fluctuated as a function of time (Fig. 4A). To examine the time evolution of astrocyte connectivity, a time series of the MCC matrices was created every minute for a period of ± 2 min relative to the focused time and compressed onto a 3D coordinate, using the local linear embedding (LLE) algorithm (Roweis and Saul 2000). The matrix's position was found to move gradually in the LLE space (Fig. 4B), indicating that the state of the astrocyte network drifted with time, engaging different functional sets of active astrocytes. Nonetheless, the network at each moment maintained small-world architectures over time in both control and tetrodotoxin-treated slices (Fig. 4C). This indicates that astrocytic clusters are, at least in part, dynamic. Indeed, some clusters emerged repeatedly (red dots in Fig. 3B), whereas others did not. On average, $44 \pm 9\%$ of the clusters appeared more than once, whereas only $18 \pm 15\%$ of the clusters appeared repeatedly in event-shuffled surrogates ($P = 0.028$, Student's t -test for a population mean). Single astrocytes participated in the clusters 4.2 ± 3.1 times. When astrocytes reappeared in another cluster, 69% of the astrocytes were coactivated with at least 1 of the astrocytes that had coparticipated in the previous cluster. This

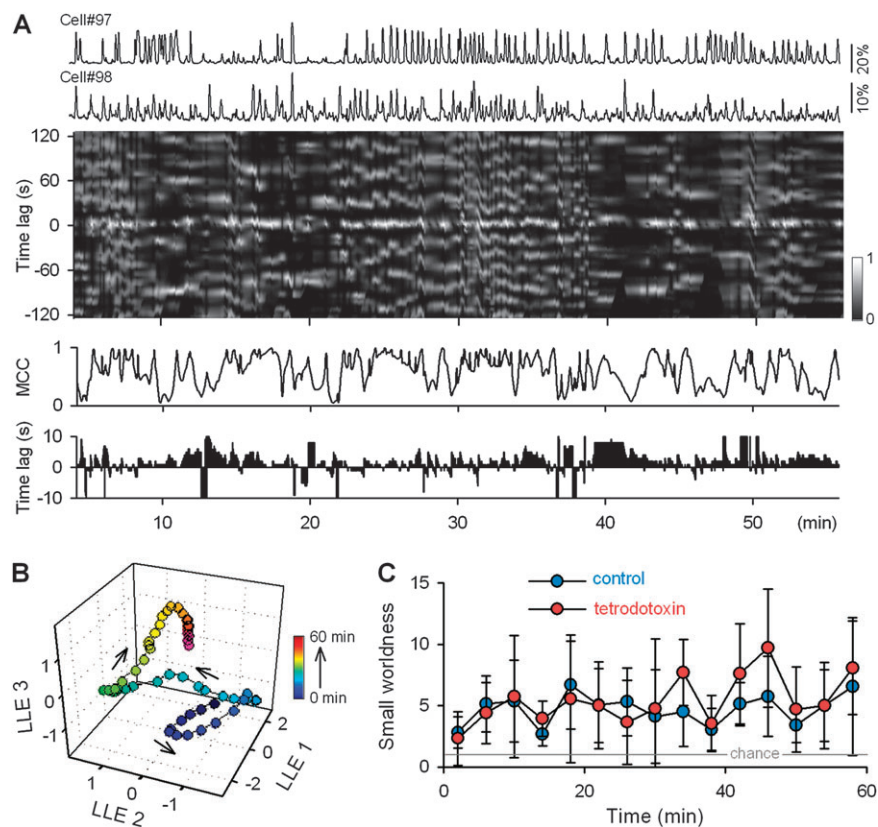


Figure 4. Temporal dynamics of astrocytic connectivity. (A) Time-dependent change in cross-correlograms (middle) between 2 traces of a representative cell pair (top). Two bottom plots indicate the MCC and its time lag at a given time. (B) Representative state changes in the time series of the MCC matrices obtained from the movie in Figure 1B. To examine the time evolution of astrocyte connectivity, a time series of the MCC matrices was created every minute for a period of ± 2 min relative to the focused time and compressed onto a 3D coordinate with the LLE algorithm. The matrix's position moved gradually in the LLE space, indicating that the state of the astrocyte network drifted with time, engaging different functional sets of coactive astrocytes. (C) Time course of the small-worldness in control ($n = 6$ slices from 6 animals) and 1 μM tetrodotoxin-treated ($n = 3$ slices from 3 animals) slices. Small-world architectures were maintained over time in both control and tetrodotoxin-treated slices.

“accompanying” ratio was also significantly higher than the level of chance ($37 \pm 2\%$ in event-shuffled surrogates, $P < 0.001$, Z-test for a population mean). All these data indicate that the spatial pattern of clusters was recursive to some extent. Our imaging period of up to 60 min, however, may be insufficient for full characterization of the long-term organization of astrocytic clusters. Further studies investigating the stability and dynamics of clusters will require a longer observation time.

Neuronal Activity-Evoked Astrocytic Calcium Events

To investigate whether neuronal activity activates astrocytes in synchrony like astrocytic clusters, we applied electric field stimulation to the Schaffer collaterals/commissural fibers (Supplementary Fig. S5A). Astrocytes located within a radius of ca. 50 μm from the electrode tip (broken line) were not used in this analysis because these cells might be activated directly by the electrical stimulation. We found that a set of astrocytes in the CA1 stratum radiatum exhibited calcium activity in response to the stimulation, resembling astrocytic clusters (Supplementary Fig. S5B,C). More cells were activated as the number of stimulation pulses increased (Supplementary Fig. S5D), consistent with reports showing that astrocytes respond to bursty, but not single, action potentials (Albensi et al. 2007; Fiacco et al. 2009). Tetrodotoxin reduced the evoked synchronous activity to a level of spontaneously occurring clusters (Supplementary Fig.

S5D). Addition of 50 μM picrotoxin, a γ -aminobutyric acid_A receptor antagonist, did not affect the synchronous activity evoked by 100-pulse stimulation (Supplementary Fig. S5D).

In Vivo Astrocyte Clusters

In vivo 2-photon imaging from the hippocampus was conducted in anesthetized mice (Fig. 5A). The alveus surface of the hippocampus was exposed by aspiration (Fig. 5B). To examine whether the aspiration altered the nature of hippocampal activity, we performed extracellular recordings of local field potentials (LFPs) from the CA1 stratum pyramidale (Supplementary Fig. S6A). The fast Fourier transform power of the LFPs revealed that the power spectrum did not significantly differ between non-aspirated (intact) and aspirated brains, whereas it was attenuated by tetrodotoxin (Supplementary Fig. S6B,C).

Spontaneous calcium activity was monitored from 101 ± 77 astrocytes (8 movies from 8 animals) (Fig. 5C). There was no statistical difference in the percentage of active astrocytes per minute or the frequency, duration, or amplitude of calcium events between the in situ and in vivo imaging results (Fig. 5D–G). Clusters were evident in the hippocampus in vivo (Fig. 5H). The number of clusters and the mean percentage of calcium transients participating in the clusters were comparable to the results obtained in situ (Fig. 3F,G vs. Fig. 5J,K). In vivo clusters were also reduced by MCPG but were resistant to tetrodotoxin (Fig. 5I–K).

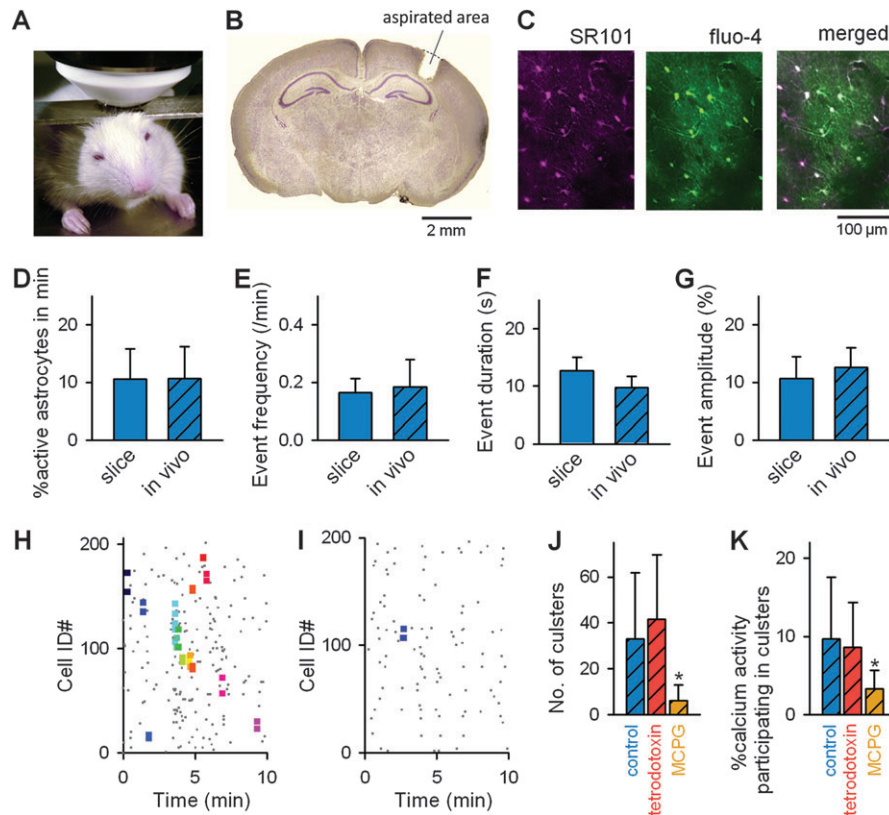


Figure 5. Activity of hippocampal astrocytes in vivo. (A) The hippocampus was imaged in a head-restrained, urethane-anesthetized mouse using 2-photon microscopy. (B) Nissl-stained coronal section in which the cerebral cortex was partially aspirated to increase optical accessibility to the hippocampus. (C) In vivo 2-photon images of cells loaded with SR101 and fluo-4. (D–G) The mean percentage of active astrocytes in a given minute (D) and the frequency (E), duration (F), and amplitude (G) of individual calcium events. Data obtained for 8 in vivo movies were compared with the in vitro data obtained for control slices (the same as in Figure 1E–H), but no statistical difference was found (Student’s *t*-test). (H, I) Representative raster plot showing astrocytic clusters in control (H) and 500 μ M MCPG-treated hippocampi (I). Clusters are indicated in colors. (J, K) The number of clusters observed per 100 cells in 60 min (J) and the percentage of the calcium transients involved in clusters (K) in control ($n = 9$ movies from 8 animals), 1 μ M tetrodotoxin-treated ($n = 8$ movies from 6 animals), and 500 μ M MCPG-treated ($n = 9$ movies from 8 animals) hippocampi. * $P < 0.05$ versus control, analysis of variance followed by Tukey’s test.

Astrocytic Cluster-Induced Depolarization of Neurons

To elucidate the biological function of astrocytic clusters, we returned to in vitro experiments using hippocampal slice preparations. We examined the resting membrane potentials of neurons during the synchronized calcium activity of astrocytes. While the membrane voltage was recorded from a neuron, the calcium activities were evoked in nearby astrocytes by uncaging calcium, mimicking the astrocytic clusters. In each experiment, a CA1 pyramidal neuron was whole-cell recorded and intracellularly visualized using Alexa Fluor 488. Then, 3 astrocytes near the proximal dendrite of the neuron were intracellularly loaded with OGB-1 and NP-EGTA through multiple patch-clamp pipettes (Fig. 6A). These experiments were repeated in all 9 slices prepared from 6 animals. UV illumination of astrocytes induced an increase in the somatic calcium fluorescence, the amplitude of which was $9.1 \pm 5.2\%$ ($n = 27$ astrocytes from 9 slices) and not statistically different from that observed during spontaneous events ($10.7 \pm 3.8\%$, $n = 1592$ cells, Fig. 1H).

For comparison to previous studies (Fiacco and McCarthy 2004; Jourdain et al. 2007; Perea and Araque 2007), we first monitored spontaneous excitatory postsynaptic potential (sEPSP) events in the current-clamped neurons. Photoactivation of astrocytes was accompanied by an increase in the frequency of sEPSPs by $60.2 \pm 87.3\%$ ($n = 9$ neurons from 6

animals), in accordance with previous studies (Fiacco and McCarthy 2004; Jourdain et al. 2007; Perea and Araque 2007). Therefore, we concluded that our procedure of UV uncaging readily replicated the data reported in these previous studies.

Under these experimental conditions, we found, in 8 of 9 slices, that the activation of 3 astrocytes induced a slight depolarization in the patched neurons. The depolarization shift was 1.5 ± 1.4 mV ($P = 0.021$, paired *t*-test, $n = 8$ experiments from 8 slices from 6 animals; Fig. 6B,C, cluster). This depolarizing effect was blocked by a cocktail of 50 μ M AP5 and 20 μ M CNQX but not by 50 μ M AP5 alone (Fig. 6C). Thus, non-NMDA ionotropic receptors mediated cluster-induced depolarization. No depolarization occurred when UV exposure was applied to slices in which NP-EGTA was not injected into astrocytes (Fig. 6B,C, UV alone) or in which NP-EGTA was injected into a single astrocyte (Fig. 6C, single cell).

Previous studies have shown that the calcium-dependent release of glutamate from astrocytes elicits NMDA receptor-dependent SICs in hippocampal neurons (Fellin et al. 2004; Shigetomi et al. 2008). In those studies, neurons were recorded in a low magnesium solution or voltage-clamped at more depolarized membrane potentials to augment NMDA receptor-mediated currents. Consistent with this, we found that when neurons were held at -30 mV, they exhibited SICs in response to the UV uncaging of even “single” astrocytes (Fig. 6D, left).

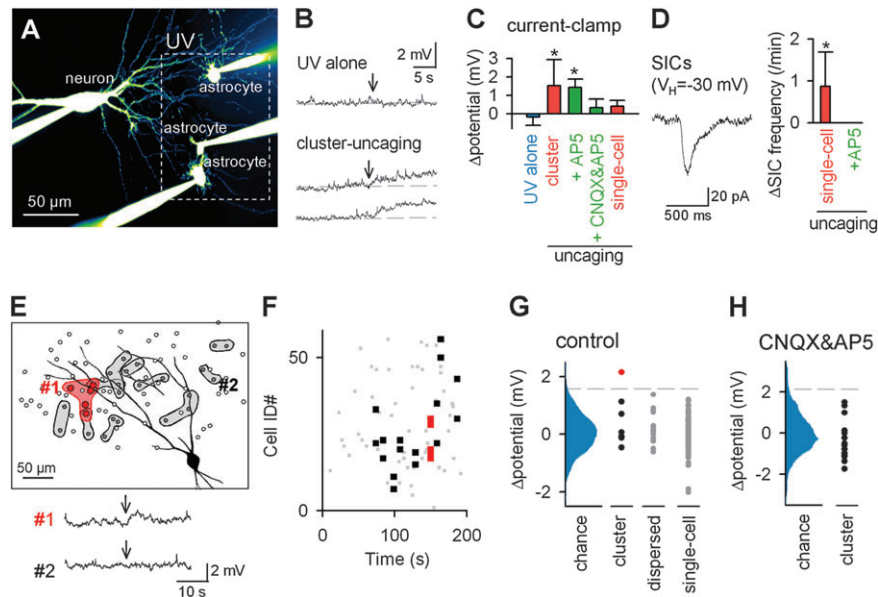


Figure 6. Cluster-induced depolarization of nearby neurons. (A) Representative confocal image showing an experiment in which 1 CA1 pyramidal cell and 3 astrocytes were whole-cell recorded. The neuron was visualized by intracellular injection of 200 μM Alexa Fluor 488 hydrazide. The astrocytes were loaded with 100 μM OGB-1 and the caged calcium 200 μM NP-EGTA. The boxed region was illuminated with UV. (B) Intracellular voltage response of the recorded neurons to UV-induced NP-EGTA photolysis (arrows). (C) Changes in the resting potential of the neurons after calcium uncaging of 3 astrocytes under control conditions (cluster, $n = 8$ experiments from 8 slices from 6 animals) and in the presence of 50 μM AP5 (+AP5, $n = 6$ experiments from 6 slices from 5 animals) and 20 μM CNQX and 50 μM AP5 (+CNQX&AP5, $n = 4$ experiments from 4 slices from 3 animals). No significant changes in neuronal membrane potentials were induced by photoactivation of single astrocytes (single cell, $n = 6$ experiments from 6 slices from 4 animals). UV light alone did not alter membrane voltages (UV alone, $n = 8$ experiments from 8 slices from 5 animals), $*P < 0.05$ versus before UV exposure, paired t -test. (D) UV activation of single astrocytes induced SICs (left) in neurons that were voltage-clamped at -30 mV ($n = 7$ experiments from 7 slices from 5 animals). No SICs occurred in the presence of 50 μM AP5 ($n = 3$ experiments from 3 slices from 2 animals). (E) A CA1 pyramidal neuron was current-clamped with an Alexa Fluor 488-loaded whole-cell pipette. Spontaneous calcium activities were monitored from surrounding astrocytes in the presence of tetrodotoxin, and clusters were detected. Representative voltage traces at the times of clusters #1 and #2 are shown in the bottom. (F) Changes in membrane potentials of the recorded neuron at the time of cluster occurrence (cluster). The left histogram indicates the distribution of background fluctuations in membrane potentials in the same dataset (chance). In panels E–G, clusters above the top 1% of the chance distribution are colored in red. (G) Distribution of changes in neuronal membrane potentials by chance (chance), at times of cluster occurrence (cluster), at times of synchronous, but not clustered, activity (dispersed), and sporadic astrocytic activities (single). (H) In the presence of 50 μM CNQX and 50 μM AP5, no clusters were found to correlate significantly with depolarization.

The SICs had the amplitude of -36 ± 12 pA, the 10% to 90% rise time of 66 ± 12 ms, the decay time of 224 ± 30 ms, and the event frequency of 1.2 ± 1.1 min^{-1} (Fig. 6D, right, $n = 6$ slices from 3 animals), and they were abolished by application of 50 μM AP5. Thus, SICs were a different phenomenon rather than the long-lasting (>3 s, >1 mV) depolarizations induced by calcium uncaging of multiple astrocytes (Fig. 6B,C).

Similar experiments were conducted with spontaneously occurring clusters. Single CA1 pyramidal neurons were current-clamped with Alexa Fluor 488-loaded pipettes. In the presence of tetrodotoxin, spontaneous calcium activities were monitored from astrocytes near the neurons, and clusters were detected (Fig. 6F). Next, we performed the “reverse-correlation” analysis for these detected clusters. This analysis consists of 3 steps: 1) to examine en masse whether any cluster induced significant depolarization in the patch-clamped neuron; 2) to identify the cluster responsible for the depolarization; and 3) to examine where the cluster occurred relative to the location of the patched neuron. Specifically, we compared the membrane potentials of the neuron between 2 time points, 3 s before and 3 s after the timing of each cluster occurrence, to determine the changes in membrane potentials caused by the cluster. The significance of the change was statistically assessed using the bootstrapping method (Henderson 2005); we determined whether the membrane potential change was significantly higher compared with a “chance” distribution, which could occur as a result of

intrinsic membrane potential fluctuations. To estimate the chance fluctuations, we collected the values of changes in membrane potentials between any given 2 time points separated by 6 s from the entire time range of the same patch-clamp recording trace. (These time points are not necessarily time locked to the clusters.) This resampling process, called bootstrapping, provides a chance distribution that represents the intrinsic membrane potential changes that can spontaneously (or stochastically) occur during a period of 6 s in the absence of external signals (Fig. 6G, chance). The top 1% level of this distribution (i.e., $P < 0.01$) was adopted as a threshold for significant depolarization (Fig. 6G, broken line).

We identified clusters that emerged when the patch-clamped neuron showed significant depolarization using this procedure (Fig. 6G, red) and examined the locations of these selected clusters. The selected clusters were found to overlap dendrites of the recorded neurons (Fig. 6E, red). We repeated this reverse-correlation analysis for 4 other slices and found that all the clusters that co-occurred with significant depolarization overlapped the neuronal dendrites. In the presence of 50 μM CNQX and 50 μM AP5, no clusters correlated significantly with the depolarization (Fig. 6H, $n = 3$ slices). We also applied this analysis to the sporadic activity of single astrocytes (single) or synchronous (but not clustered) activity of sparsely distributed astrocytes (dispersed). We failed to find evidence that these activity patterns triggered any significant

depolarization (Fig. 6G). Thus, either single astrocytic activity or synchronous activity of multiple astrocytes is insufficient to depolarize neurons, but rather, the spatial structure in the activation of multiple astrocytes is crucial. Given that astrocytic activities tended to be spatially grouped at a level that exceeds chance, we conclude that astrocytic clusters are a biologically significant phenomenon.

Discussion

We carried out large-scale optical recordings of astrocytic calcium activity and discovered the hitherto unknown complex dynamics of spontaneous calcium transients organized into locally synchronized clusters.

A well-characterized form of multiastrocytic activity is the calcium wave that travels from cell to cell with a delay of tens of seconds. The calcium wave has been observed in cell culture preparations (Cornell-Bell et al. 1990; Charles et al. 1991; Araque et al. 1998b) and organotypic brain slices (Dani et al. 1992; Harris-White et al. 1998). We failed to observe such widespread activity propagations, but we discovered time-lag calcium correlations of close to zero. Although the correlated activity between neighboring pairs of astrocytes has been implied in acute hippocampal slices (Aguado et al. 2002) and in the neocortex in vivo (Hirase et al. 2004; Takata and Hirase 2008; Kuchibhotla et al. 2009), we performed much larger-scale imaging and found that the correlated activities consisted of multiple astrocytes that were organized into ensemble dynamics, like a slow-kinetics version of neuronal cell assemblies (Harris 2005). We termed this new form of multiple astrocyte dynamics “clusters.”

Astrocytic clusters may have been overlooked because of the smaller-scale imaging techniques used in previous studies. This hypothesis is supported by a computational simulation in which we attempted to find clusters after scaling down our large datasets of astrocytic activity (Supplementary Fig. S7). As expected, the probability of encountering clusters increased with the length of the movie and the number of imaged astrocytes; conventional imaging sizes were almost below the lower limits of detection. It is possible, however, that even our imaging technique still underestimated the frequency and size of the clusters due to the optical 2D sectioning. Using another computer simulation, we extrapolated our 2D datasets into 3D space and estimated the actual number the clusters (Supplementary Fig. S8). In realistic 3D tissues, the number of cells involved in single clusters would range from 2 to 10 cells (Supplementary Fig. S8E), and $59 \pm 3\%$ of the observed calcium events could involve clusters ($n = 100$ simulations, Supplementary Fig. S8F).

Cluster activity was mediated by metabotropic glutamate receptors but not NMDA receptors, gap junctions, or purinergic receptors. Given that the clusters were independent of neuronal activity, glutamate released from astrocytes are likely to activate metabotropic glutamate receptors present on astrocytes (Aguilhon et al. 2008). Astrocytes express mGluR3 and mGluR5 (Testa et al. 1994), and these receptor subtypes may contribute to cluster generation. Astrocytic clusters, however, can be explained by another possibility that “dead” axons in slice preparations release glutamate and induce synchronized activation of nearby astrocytes. This mechanism seems unlikely because of 2 observations. First, the frequency of astrocytic clusters did not differ between slice preparations

and in vivo animals (Fig. 5). Second, astrocytic clusters were repetitively replayed; $44 \pm 9\%$ of the clusters emerged repeatedly, and 69% of the astrocytes were coactivated with at least 1 of the astrocytes. The consistency in the activity patterns is inconsistent with the idea that clusters are formed by extracellularly released glutamate at the time of the death of individual axons. The plasma membrane of an astrocyte expresses high-affinity glutamate transporters at a density of up to $10\,000\ \mu\text{m}^{-2}$ (Danbolt 2001). These transporters not only terminate excitatory synaptic transmission but also prevent the spillover of glutamate released by neurons and astrocytes. Therefore, local and transient downregulation of glutamate uptake may facilitate the generation of astrocytic clusters.

We utilized preparations from early postnatal brains (P9–12 mice), in which astrogliogenesis still continues (Sauvageot and Stiles 2002), and the extracellular space is larger compared with that in the adult brain (Sykova and Nicholson 2008). In addition, the expression level of glutamate transporters at this developmental stage does not reach the mature level (Kugler and Schleyer 2004). Therefore, astrocytic clusters may represent phenomena related to development of immature cells. It remains to be tested whether astrocytic clusters are a phenomenon that persists into the adulthood because we were not able to conduct calcium imaging using mature brain preparations due to the low efficiency of calcium dye loading in adult brain tissues.

Neurons were depolarized via non-NMDA receptors when clusters appeared near their dendrites. Importantly, the activation of a single astrocyte did not exert the same effect but readily elicited NMDA receptor-dependent SICs. Therefore, the synchronization of a few nearby astrocytes is required to elevate extracellular glutamate concentrations to a degree adequate for activation of non-NMDA receptors, whereas the activation of a single astrocyte is sufficient to activate NMDA receptors when the neurons are depolarized (Fellin et al. 2004; Mothet et al. 2005; Shigetomi et al. 2008; Henneberger et al. 2010). This finding is in accordance with the observation that NMDA receptors possess about 100 times higher glutamate affinity than do AMPA receptors (Meldrum 2000). Thus, clusters and the sporadic activity of astrocytes will play different roles in the function of the neuronal network. We speculate that clusters enhance the local excitability of neuronal networks by inducing tonic depolarization of neurons, whereas sporadic activity lowers the threshold of synaptic plasticity by enhancing NMDA receptor activity.

Finally, monitoring somatic calcium activity alone may not capture the calcium dynamics of astrocytes because a single astrocyte seems to include multiple subcellular domains of calcium hot spots (Nett et al. 2002; Shigetomi et al. 2008, 2010). For example, our low spatial resolution imaging technique using a low-magnification objective lens ($\times 10$ – 20), which is necessary for imaging from large cell populations, cannot resolve whether the somatic calcium activity are synchronized with calcium in astrocytic processes. Further establishing new techniques with higher spatiotemporal resolutions will provide more accurate information about the dynamics and function of astrocytes.

Supplementary Material

Supplementary material can be found at: <http://www.cercor.oxfordjournals.org/>.

Funding

This work was supported in part by a Grant-in-Aid for Science Research (KAKENHI# 22650080, 22680025).

Notes

Conflict of Interest: None declared.

References

- Aguado F, Espinosa-Parrilla JF, Carmona MA, Soriano E. 2002. Neuronal activity regulates correlated network properties of spontaneous calcium transients in astrocytes in situ. *J Neurosci*. 22:9430-9444.
- Agulhon C, Fiacco TA, McCarthy KD. 2010. Hippocampal short- and long-term plasticity are not modulated by astrocyte Ca^{2+} signaling. *Science*. 327:1250-1254.
- Agulhon C, Petravic J, McMullen AB, Sweger EJ, Minton SK, Taves SR, Casper KB, Fiacco TA, McCarthy KD. 2008. What is the role of astrocyte calcium in neurophysiology? *Neuron*. 59:932-946.
- Albensi BC, Oliver DR, Toupin J, Odero G. 2007. Electrical stimulation protocols for hippocampal synaptic plasticity and neuronal hyperexcitability: are they effective or relevant? *Exp Neurol*. 204: 1-13.
- Angulo MC, Kozlov AS, Charpak S, Audinat E. 2004. Glutamate released from glial cells synchronizes neuronal activity in the hippocampus. *J Neurosci*. 24:6920-6927.
- Araque A, Parpura V, Sanzgiri RP, Haydon PG. 1998a. Glutamate-dependent astrocyte modulation of synaptic transmission between cultured hippocampal neurons. *Eur J Neurosci*. 10:2129-2142.
- Araque A, Sanzgiri RP, Parpura V, Haydon PG. 1998b. Calcium elevation in astrocytes causes an NMDA receptor-dependent increase in the frequency of miniature synaptic currents in cultured hippocampal neurons. *J Neurosci*. 18:6822-6829.
- Bushong EA, Martone ME, Jones YZ, Ellisman MH. 2002. Protoplasmic astrocytes in CA1 stratum radiatum occupy separate anatomical domains. *J Neurosci*. 22:183-192.
- Charles AC, Merrill JE, Dirksen ER, Sanderson MJ. 1991. Intercellular signaling in glial cells: calcium waves and oscillations in response to mechanical stimulation and glutamate. *Neuron*. 6:983-992.
- Cornell-Bell AH, Finkbeiner SM, Cooper MS, Smith SJ. 1990. Glutamate induces calcium waves in cultured astrocytes: long-range glial signaling. *Science*. 247:470-473.
- Danbolt NC. 2001. Glutamate uptake. *Prog Neurobiol*. 65:1-105.
- Dani JW, Chernjavsky A, Smith SJ. 1992. Neuronal activity triggers calcium waves in hippocampal astrocyte networks. *Neuron*. 8: 429-440.
- Fellin T, Pascual O, Gobbo S, Pozzan T, Haydon PG, Carmignoto G. 2004. Neuronal synchrony mediated by astrocytic glutamate through activation of extrasynaptic NMDA receptors. *Neuron*. 43:729-743.
- Fiacco TA, Agulhon C, McCarthy KD. 2009. Sorting out astrocyte physiology from pharmacology. *Annu Rev Pharmacol Toxicol*. 49: 151-174.
- Fiacco TA, Agulhon C, Taves SR, Petravic J, Casper KB, Dong X, Chen J, McCarthy KD. 2007. Selective stimulation of astrocyte calcium in situ does not affect neuronal excitatory synaptic activity. *Neuron*. 54:611-626.
- Fiacco TA, McCarthy KD. 2004. Intracellular astrocyte calcium waves in situ increase the frequency of spontaneous AMPA receptor currents in CA1 pyramidal neurons. *J Neurosci*. 24:722-732.
- Frey BJ, Dueck D. 2007. Clustering by passing messages between data points. *Science*. 315:972-976.
- Hamilton NB, Attwell D. 2010. Do astrocytes really exocytose neurotransmitters? *Nat Rev Neurosci*. 11:227-238.
- Harris KD. 2005. Neural signatures of cell assembly organization. *Nat Rev Neurosci*. 6:399-407.
- Harris-White ME, Zanotti SA, Frautschy SA, Charles AC. 1998. Spiral intercellular calcium waves in hippocampal slice cultures. *J Neurophysiol*. 79:1045-1052.
- Henderson AR. 2005. The bootstrap: a technique for data-driven statistics. Using computer-intensive analyses to explore experimental data. *Clin Chim Acta*. 359:1-26.
- Henneberger C, Papouin T, Oliet SH, Rusakov DA. 2010. Long-term potentiation depends on release of D-serine from astrocytes. *Nature*. 463:232-236.
- Hirase H, Qian L, Bartho P, Buzsaki G. 2004. Calcium dynamics of cortical astrocytic networks in vivo. *PLoS Biol*. 2:e96.
- Hoogland TM, Kuhn B, Gobel W, Huang W, Nakai J, Helmchen F, Flint J, Wang SS. 2009. Radially expanding transglial calcium waves in the intact cerebellum. *Proc Natl Acad Sci U S A*. 106:3496-3501.
- Humphries MD, Gurney K, Prescott TJ. 2006. The brainstem reticular formation is a small-world, not scale-free, network. *Proc Biol Sci*. 273:503-511.
- Ikegaya Y, Aaron G, Cossart R, Aronov D, Lampl I, Ferster D, Yuste R. 2004. Synfire chains and cortical songs: temporal modules of cortical activity. *Science*. 304:559-564.
- Jourdain P, Bergersen LH, Bhaukaurally K, Bezzi P, Santello M, Domercq M, Matute C, Tonello F, Gundersen V, Volterra A. 2007. Glutamate exocytosis from astrocytes controls synaptic strength. *Nat Neurosci*. 10:331-339.
- Kang J, Jiang L, Goldman SA, Nedergaard M. 1998. Astrocyte-mediated potentiation of inhibitory synaptic transmission. *Nat Neurosci*. 1:683-692.
- Koyama R, Muramatsu R, Sasaki T, Kimura R, Ueyama C, Tamura M, Tamura N, Ichikawa J, Takahashi N, Usami A, et al. 2007. A low-cost method for brain slice cultures. *J Pharmacol Sci*. 104:191-194.
- Kuchibhotla KV, Lattarulo CR, Hyman BT, Bacskaï BJ. 2009. Synchronous hyperactivity and intercellular calcium waves in astrocytes in Alzheimer mice. *Science*. 323:1211-1215.
- Kuga N, Sasaki T, Takahara Y, Matsuki N, Ikegaya Y. 2011. Large-scale calcium waves traveling through astrocytic networks in vivo. *J Neurosci*. In press.
- Kugler P, Schleyer V. 2004. Developmental expression of glutamate transporters and glutamate dehydrogenase in astrocytes of the postnatal rat hippocampus. *Hippocampus*. 14:975-985.
- Latora V, Marchiori M. 2001. Efficient behavior of small-world networks. *Phys Rev Lett*. 87:198701.
- Meldrum BS. 2000. Glutamate as a neurotransmitter in the brain: review of physiology and pathology. *J Nutr*. 130:1007S-1015S.
- Mizrahi A, Crowley JC, Shtoyerman E, Katz LC. 2004. High-resolution in vivo imaging of hippocampal dendrites and spines. *J Neurosci*. 24: 3147-3151.
- Mothet JP, Pollegioni L, Ouanounou G, Martineau M, Fossier P, Baux G. 2005. Glutamate receptor activation triggers a calcium-dependent and SNARE protein-dependent release of the gliotransmitter D-serine. *Proc Natl Acad Sci U S A*. 102:5606-5611.
- Namiki S, Matsuki N, Ikegaya Y. 2009. Large-scale imaging of brain network activity from >10,000 neocortical cells. *Nature Precedings*. Available from: URL <http://precedings.nature.com/documents/2893/>.
- Nett WJ, Oloff SH, McCarthy KD. 2002. Hippocampal astrocytes in situ exhibit calcium oscillations that occur independent of neuronal activity. *J Neurophysiol*. 87:528-537.
- Nimmerjahn A, Kirchhoff F, Kerr JN, Helmchen F. 2004. Sulforhodamine 101 as a specific marker of astroglia in the neocortex in vivo. *Nat Methods*. 1:31-37.
- Nimmerjahn A, Mukamel EA, Schnitzer MJ. 2009. Motor behavior activates Bergmann glial networks. *Neuron*. 62:400-412.
- Ogata K, Kosaka T. 2002. Structural and quantitative analysis of astrocytes in the mouse hippocampus. *Neuroscience*. 113:221-233.
- Perea G, Araque A. 2005. Properties of synaptically evoked astrocyte calcium signal reveal synaptic information processing by astrocytes. *J Neurosci*. 25:2192-2203.
- Perea G, Araque A. 2007. Astrocytes potentiate transmitter release at single hippocampal synapses. *Science*. 317:1083-1086.
- Porter JT, McCarthy KD. 1996. Hippocampal astrocytes in situ respond to glutamate released from synaptic terminals. *J Neurosci*. 16: 5073-5081.
- Roweis ST, Saul LK. 2000. Nonlinear dimensionality reduction by locally linear embedding. *Science*. 290:2323-2326.
- Royer L, Reimann M, Andreopoulos B, Schroeder M. 2008. Unraveling protein networks with power graph analysis. *PLoS Comput Biol*. 4:e1000108.

- Sasaki T, Matsuki N, Ikegaya Y. 2007. Metastability of active CA3 networks. *J Neurosci.* 27:517-528.
- Sauvageot CM, Stiles CD. 2002. Molecular mechanisms controlling cortical gliogenesis. *Curr Opin Neurobiol.* 12:244-249.
- Shigetomi E, Bowser DN, Sofroniew MV, Khakh BS. 2008. Two forms of astrocyte calcium excitability have distinct effects on NMDA receptor-mediated slow inward currents in pyramidal neurons. *J Neurosci.* 28:6659-6663.
- Shigetomi E, Kracun S, Sofroniew MV, Khakh BS. 2010. A genetically targeted optical sensor to monitor calcium signals in astrocyte processes. *Nat Neurosci.* 13:759-766.
- Song S, Sjöström PJ, Reigl M, Nelson S, Chklovskii DB. 2005. Highly nonrandom features of synaptic connectivity in local cortical circuits. *PLoS Biol.* 3:e68.
- Sykova E, Nicholson C. 2008. Diffusion in brain extracellular space. *Physiol Rev.* 88:1277-1340.
- Takata N, Hirase H. 2008. Cortical layer 1 and layer 2/3 astrocytes exhibit distinct calcium dynamics in vivo. *PLoS One.* 3:e2525.
- Testa CM, Catania MV, Young AB, editors. Anatomical distribution of metabotropic glutamate receptors in mammalian brain. Totowa (NJ): Humana Press.
- Tian GF, Azmi H, Takano T, Xu Q, Peng W, Lin J, Oberheim N, Lou N, Wang X, Zielke HR, et al. 2005. An astrocytic basis of epilepsy. *Nat Med.* 11:973-981.
- Wang X, Lou N, Xu Q, Tian GF, Peng WG, Han X, Kang J, Takano T, Nedergaard M. 2006. Astrocytic Ca²⁺ signaling evoked by sensory stimulation in vivo. *Nat Neurosci.* 9:816-823.
- Watts DJ, Strogatz SH. 1998. Collective dynamics of 'small-world' networks. *Nature.* 393:440-442.
- Weber PA, Chang HC, Spaeth KE, Nitsche JM, Nicholson BJ. 2004. The permeability of gap junction channels to probes of different size is dependent on connexin composition and permeant-pore affinities. *Biophys J.* 87:958-973.

Locally synchronized astrocytes

Takuya Sasaki, Nahoko Kuga, Shigehiro Namiki, Norio Matsuki, and Yuji Ikegaya

This file includes:

8 Supplemental Figures

Legends of 2 Movies

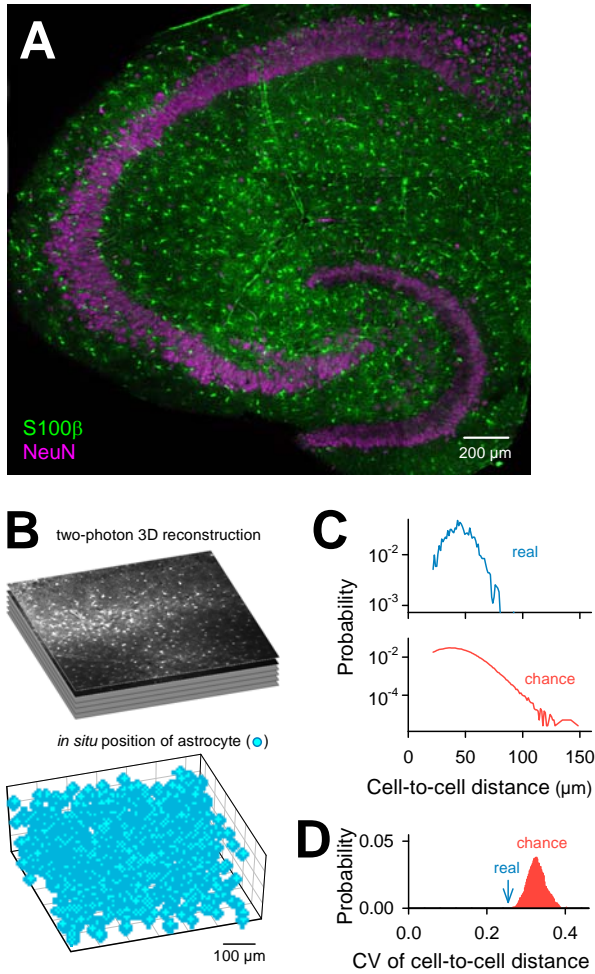


Fig. S1. Uniform distribution of astrocytes in the hippocampus. (A) Example of a mouse hippocampal slice immunostained with anti-S100 β (green) and anti-NeuN (magenta). (B) S100 β -positive astrocytes in CA1 stratum radiatum were two-photon imaged to a depth of 200 μ m from the slice surface (top) and three-dimensionally mapped (bottom). (C) Distribution of the cell-to-cell distances between the closest pairs of astrocytes in real datasets ($n = 2731$ cells from 4 slices from 3 animals) and the corresponding 1000 random surrogates. The Euclidean distance from a given cell to the nearest cell (cell-to-cell distance) was measured for all cells and compared its distribution to 1000 surrogates in which the same number of cells were scattered randomly in the same three-dimensional space, with the minimal cell-to-cell distance being 20 μ m. In the real datasets, the distribution centered on a sharper peak ($P < 0.01$, Kolmogorov-Smirnov test). (D) The coefficient of variation (CV) of the cell-to-cell distance was significantly lower than that in their random surrogates ($P < 0.001$). Thus, astrocytes are positioned evenly, rather than

randomly, in the stratum radiatum.

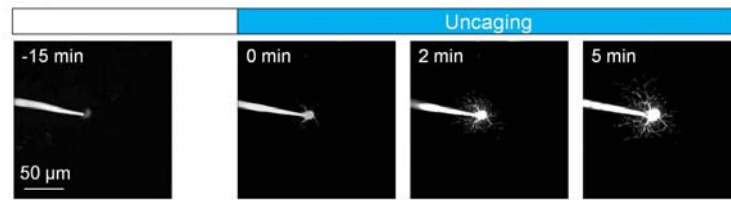


Fig. S2. No leak of fluorescent dyes loaded intracellularly into astrocytes. After OGB-1 and NP-EGTA were both injected into an astrocyte through a whole-cell patch-clamp pipette at -15 min, no leak or spreading of the OGB-1 fluorescence from the patch-clamped cell was detected at 0 min. UV illumination was started at 0 min. The UV photolysis of NP-EGTA induced an increase in the calcium fluorescence, but the increased fluorescence still stayed inside the cell at 2 and 5 min.

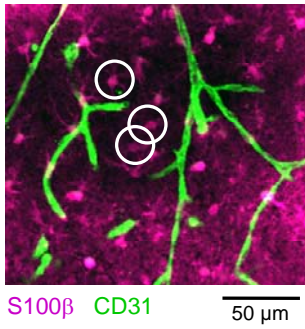


Fig. S3. No geometrical relationship between astrocytic clusters and the surrounding blood vessel alignments. An example of a mouse hippocampal slice post-hoc immunostained with anti-CD31 (green) and anti-S100 β (magenta). Astrocytes that participated in single clusters are indicated by circles. There was no apparent spatial correlation of clusters and vessels. Similar results were obtained in three other slices.

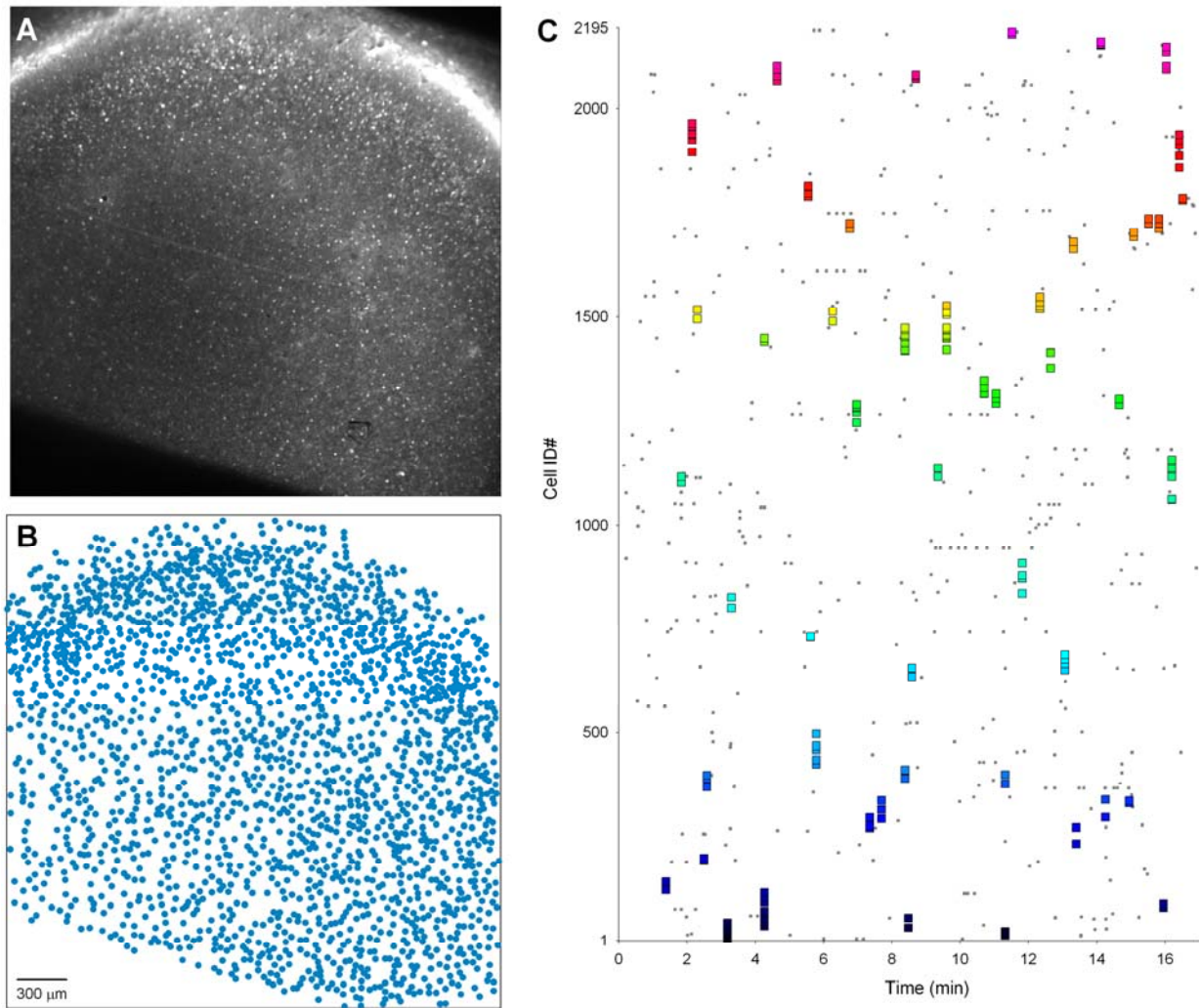


Fig. S4. Clusters of neocortical astrocytes. Representative data of calcium activity of astrocytes in a P9 mouse frontal cortical slice, in which 2195 cells were monitored for 17 min. Some cells showed spatially clustered synchronization of calcium activity, *i.e.*, clusters. The cell ID numbers were assigned so that nearby cells were closely numbered. (A) Confocal image taken at 1 Hz with a 4× objective. (B) Location of identified cells. (C) Rastergram of calcium activity. Sets of color squares indicate clusters. The movie is partly shown in Movie 2.

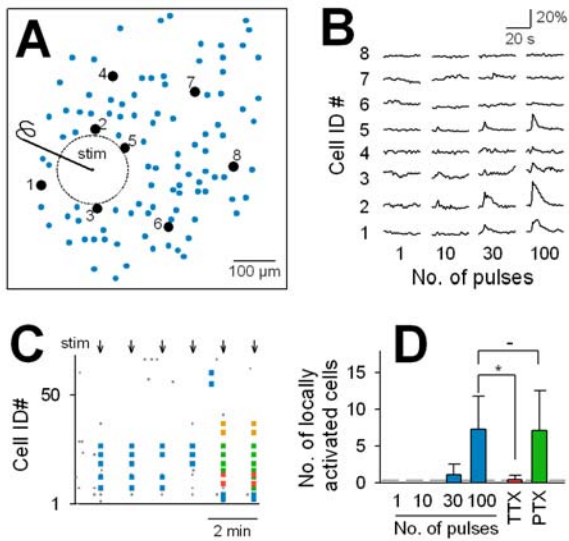


Fig. S5. Neuronal activity-evoked synchronous activation of astrocytes (A) Representative cell map of astrocytes around the tip of a stimulating electrode placed on the CA1 stratum radiatum. Astrocytes located within a radius of ~50 μm from the electrode tip (broken line) were not analyzed, because these cells might be directly activated by electric stimulation. (B) Representative fluorescence traces of 8 randomly

selected cells in response to 1-pulse, 10-pulse, 30-pulse, and 100-pulse stimulation. Note that not only the number of activated cells but also the amplitude of each calcium transient increased with the number of stimulation pulses. The degree of neuronal activity may be registered in an analog form of the astrocytic calcium signal intensity. (C) Raster plot of 100-pulse stimulation-evoked astrocytic activity, in which each color indicates a single subgroup of locally activated astrocytes (within inter-cell intervals of 50 μm, *i.e.*, the definition of a 'cluster'). Arrows indicate the stimulation timings. (D) Summary of the number of cells involved in stimulation-evoked subgroups (1, 10, 30, and 100 pulses, $n = 8-12$ slices 5 animals). Stimulation of 100 pulses was also applied in the presence of 1 μM tetrodotoxin ($n = 4$ slices from 2 animals) or 50 μM picrotoxin ($n = 4$ slices from 2 animals). Gray broken line indicates the spontaneous level. $*P < 0.05$, Welch test.

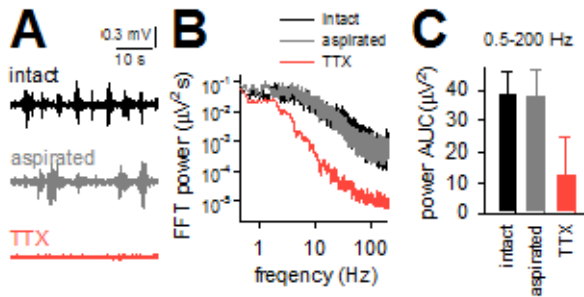


Fig. S6. No effect of neocortex aspiration on hippocampal LFPs. (A) Representative traces of LFPs recorded from the CA1 stratum pyramidale in an intact 'not-aspirated' brain and control or TTX-treated 'aspirated' brain. (B) Fast-Fourier transform (FFT) of LFPs shown in (A). (C) The area under the curves (AUCs) of the FFT power in the ranges of 0.1–200 Hz in intact brains ($n = 4$ animals) and control ($n = 3$ animals) or TTX-treated aspirated brains ($n = 2$ animals).

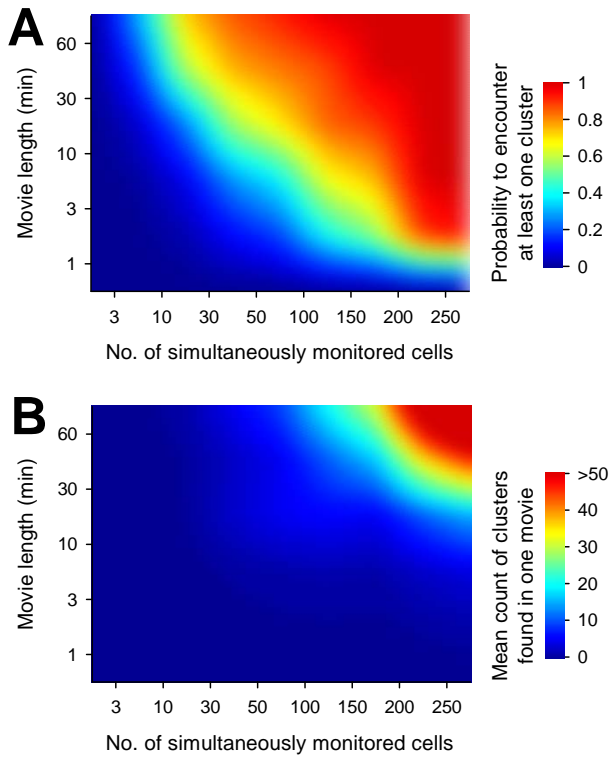


Fig. S7. Requirement of large-scale imaging for reliable cluster detection (computer simulation). To examine whether clusters are detectable with conventional "small-scale" imaging techniques, we scaled down our large raster plots of astrocytic activity by randomly cropping them in space and time ($n = 9$ control slices from 7 animals) and tried to detect clusters in these scaled-down datasets. The probability to detect at least one cluster (A) and the number of the detected clusters (B) are plotted as dual functions of the number of simultaneously monitored cells and the movie length. The plots indicate that reliable cluster detection requires sufficiently large-scale imaging. This is probably a reason why clusters have been overlooked by conventional small-scale imaging techniques.

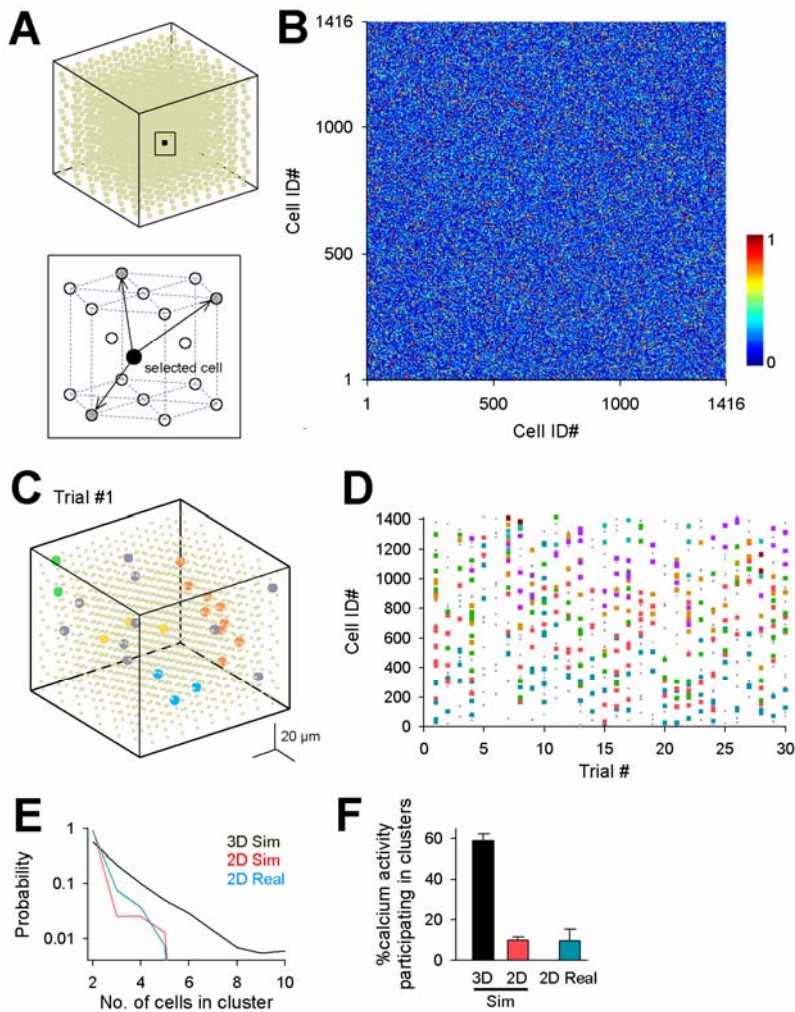


Fig. S8. Three-dimensional estimation of astrocytic clusters (computer simulation). In our confocal imaging, clusters were captured only in confocally sectioned 2D planes. Thus we might underestimate the frequency and size of the clusters. To estimate the actual degree of cluster activity, we generated "artificial" clusters in a "virtual" 3D space and sectioned this space at randomly selected "virtual" confocal planes. (A) Schematic illustration for the percolation simulation. In a $450 \times 450 \times 450 \mu\text{m}$ cubic space, 1416 "virtual" astrocytes were placed at the apexes of a hexagonal closest-packed lattice (left). In each trial, one cell is randomly chosen. For example, the cell selected in a trial is indicated in the black box, which is magnified in the bottom inset. This cell stochastically activates

cells along its MCC-weighted edges (arrows). The gray circles indicate activated neighbors. (B) Representative MCC matrix of three-dimensionally aligned astrocytes, which was computer-generated based on the results of Figure 2B. (C) Activation pattern in the trial #1. Each color indicates a single cluster, whereas cells that did not participate in any clusters are indicated in gray. (D) Raster plot of the first 30 trials of the simulations. Clusters are indicated by colors. (E, F) Distribution of the number of cells involved in single clusters (E) and the mean percentage of calcium transients used in clusters to the total (F) in 100 trials of three-dimensional simulations (3D Sim), single "pseudo-confocal" planes obtained from the simulation (2D Sim), and real data taken from 10 hippocampal slices (2D Real). Within the pseudo-confocal planes, we adjusted the parameters of simulated clusters to those of our "real" datasets and then calculated backward the cluster level in the 3D space (E and F). As a result, we estimated that, in 3D tissues, the number of cells that constituted single clusters was 2.9 ± 1.4 cells, ranging from 2 to 10 cells (E) and that $58.9 \pm 3.4\%$ calcium events were parts of clusters (F).

Movie 1. Spontaneous calcium activity of hippocampal astrocytes. The first half is a raw fluorescence movie, and the second half represents a $\Delta F/F$ movie with synchronous activity clusters being circled. The movie speed is 100-fold faster than real time. The movie size corresponds to a rectangle of $520 \mu\text{m} \times 400 \mu\text{m}$.

Movie 2. Spontaneous calcium activity of astrocytes in a prefrontal cortical slice. The movie speed is 100-fold faster than real time. The movie size corresponds to a rectangle of $2800 \mu\text{m} \times 1900 \mu\text{m}$.